


Using resistor network models to predict the transport properties of solid-state battery composites

Received: 16 June 2024

Lukas Ketter^{1,2}, Niklas Greb¹, Tim Bernges¹ & Wolfgang G. Zeier^{1,2,3} 

Accepted: 20 January 2025

Published online: 06 February 2025

 Check for updates

Solid-state batteries use composites of solid ion conductors and active materials as electrode materials. The effective transport of charge carriers and heat thereby strongly determines the overall solid-state battery performance and safety. However, the phase space for optimization of the composition of solid electrolyte, active material, additive is too large to cover experimentally. In this work, a resistor network model is presented that successfully describes the transport phenomena in solid-state battery composites, when benchmarked against experimental data of the electronic, ionic, and thermal conductivity of $\text{LiNi}_{0.83}\text{Co}_{0.11}\text{Mn}_{0.06}\text{O}_2\text{-Li}_6\text{PS}_5\text{Cl}$ positive electrode composites. To highlight the broadness of the approach, literature data are examined using the proposed model. As the model is easily accessible and expandable, without the need for high computing power, it offers valuable guidance for experimentalists helping to streamline the tedious process of performing a multitude of experiments to understand and optimize the effective transport of composite electrodes.

Lithium-ion batteries are an inevitable part of energy storage in our modern world. However, conventional lithium-ion batteries are expected to run into performance limits¹. To push battery performance beyond these limitations, it is critical to investigate alternative battery technologies. One particularly promising technology is solid-state batteries (SSB). By replacing separators and liquid electrolytes of lithium-ion batteries with solid-state ion conductors, the usage of Li-metal negative electrodes and thus higher energy densities can potentially be enabled^{2–4}. Further advantages are increased mechanical stability, the absence of leakage and a potentially improved thermal safety⁵.

Solid-state batteries utilize composite electrodes, consisting of the electrochemically active material, the solid electrolyte (SE) and, if necessary, additives such as binders or conductive carbons, e.g., vapor grown carbon fibers (VGCF). In these composite systems, a sufficiently high ionic (σ_{ion}) and electronic (σ_{e}) conductivity are necessary, given that both charge carriers need to access the active material during the charging and discharging reactions. Since a large mismatch in effective

ionic and electronic conductivity leads to inhomogeneous reaction rates throughout the whole electrode thickness, balancing of the two transport quantities is of paramount importance to enable high electrode utilizations and avoid reaction fronts during battery operation^{6,7}.

On the one hand, charge carrier transport can be decisively influenced by varying the volumetric ratios of the electrode components given that the electrochemically active material and carbon additives are solely responsible for the electronic conduction, while the solid electrolyte exclusively conducts ions^{8,9}. With that, altering the SE content in composite anodes, such as $\text{Li}_4\text{Ti}_5\text{O}_{12}\text{-Li}_7\text{P}_2\text{S}_8\text{I-C}^{10}$ or $\text{Si-Li}_6\text{PS}_5\text{Cl (LPSCI)-C}^{11}$, can facilitate changes in the effective ionic conductivity over orders of magnitude. Similarly strong correlations between effective ionic and electronic conductivity and the volumetric ratios of the composite components were found in cathode systems such as NCM622-LPSCI^{12} , $\text{LiMn}_2\text{O}_4\text{-Li}_3\text{InCl}_6^{13}$ and S-LPSCI-C^{14} . On the other hand, the microstructure of the composite electrode can influence its effective conductivities. Froboese et al.¹⁵ demonstrated the influence of differently sized inclusions on the effective ionic

¹Institute of Inorganic and Analytical Chemistry, University of Münster, 48149 Münster, Germany. ²International Graduate School of Battery Chemistry, Characterization, Analysis, Recycling and Application (BACCARA), University of Münster, 48149 Münster, Germany. ³Forschungszentrum Jülich GmbH, Institute of Energy and Climate Research Helmholtz-Institute Münster (IMD-4), 52425 Jülich, Germany. ✉e-mail: wzeier@uni-muenster.de

conductivity of composites. Studies investigating the effect of changing active material particle sizes in NCM622-LPSCI¹⁶ and Si-LPSCI-C¹⁷ electrodes on the battery performance highlight the importance of carefully designing microstructures to improve electrode utilizations. In a similar manner, optimizing the particle size of the SE in LiNi_{0.83}Co_{0.11}Mn_{0.06} (NCM83)-LPSCI¹⁸ composites leads to better electrode utilizations due to a more homogeneous ion current distribution during battery operation. This emphasizes that both the active material and electrolyte particle size need to be considered in electrode design.

While the influence of volume fractions and microstructure on charge carrier transport is frequently investigated, the influence on the thermal transport properties is scarcely studied^{19–21}. Nonetheless, due to internal resistances (R) within the solid-state battery system, Joule heating occurs during battery operation. This is of particular importance during fast charging, as the power of heating (P) is related to the square of the applied current (I) via $P = R \cdot I^2$ ²². When the generation of thermal energy is faster than its dissipation, heat accumulates in the battery system leading to an increase of the battery temperature and the development of temperature gradients²³. This heating and temperature evolution within a cell can significantly impact battery performance, accelerate degradation kinetics and lead to at-times violent device failure^{24,25}. Particularly considering battery safety, thermal transport is known to play a critical role in conventional batteries^{22,26}. Even though solid-state batteries are often promoted as being safer than their conventional Li-ion counterparts, potential safety concerns should not be overlooked and carefully studied. Using thermodynamic models, Bates et al.²⁷ showed, that under short-circuit conditions larger temperature increases are possible in SSB compared to batteries with liquid electrolytes. Furthermore, severe reactions and fire generation even under inert atmospheres were observed by Kim et al.^{25,28} when they exposed charged cathode composites to elevated temperatures above 150 °C. This is further corroborated by exothermic reactions that were observed between SSB-components in a differential scanning calorimetry study by Johnson et al.²⁹ Especially regarding the thermal management design, thermal transport considerations for SSB pose an essential addition to the often-conducted ionic and electronic conductivity studies. Thermal transport investigations on various SE have shown that their thermal conductivities are low and show a “glass-like” temperature-dependence²¹. Density dependent thermal transport investigations on sulfidic Li⁺³⁰ and Na⁺³¹ conducting SE revealed further lowering of the thermal conductivity with porosity, leading to thermal

conductivities in the range of liquid electrolytes. The low thermal conductivity of SE materials indicate that slow heat dissipation and potential thermal runaway warrant careful consideration.

Generally, evaluating transport in composites as a function of composition relies on a variety of measurements, making them a time-consuming endeavor. These measurements are tedious considering that processing, additives, binders, and any microstructural changes will influence the effective transport through the composite and that transport needs to be re-evaluated every time. Aside from experimental approaches, microstructure-based simulations can offer valuable guidance when developing microstructural design concepts. Considering the meso- and even atomistic scale, Heo et al.³² investigated the impact of microstructure on ionic conductivity in Li₇La₃Zr₂O₁₂ computationally, while Haruyama et al.³³ calculated optimized structures and properties of interfaces between oxidic cathode active material (CAM) and β -Li₃PS₄ using density functional theory. Microstructural modelling of entire composite cathodes can further reveal percolation behavior of ion- and electron-conducting clusters⁸, while effective electronic and ionic conductivities can be calculated using flux-based simulations on composite microstructure representations^{9,34}. Finsterbusch et al.³⁵ constructed a virtual twin based on scanning electron microscopy micrographs and subsequently simulated discharge curves. Extending this approach, Chen et al.³⁶ utilized an electrochemical-thermal coupled model to simulate heat evolution in addition to discharge characteristics of composite cathodes. Nevertheless, these approaches are often computationally expensive, and a faster predictive approach is desirable to screen the transport of new systems.

In this work, we propose a simple resistor network model describing transport in solid-state battery electrode composites based on simple voxel structures that is then benchmarked against experimental transport in NCM83-LPSCI cathode composites. A schematic two-dimensional representation of a typical solid-state composite cathode microstructure in comparison to a voxel microstructure analogue is shown Fig. 1. Despite this simplification, essential concepts like tortuosity and domain size are reflected by the model. Concluding the experimental characterization and microstructure-based transport simulations of the ionic, electronic, and thermal transport properties of the NCM83-LPSCI system, the proposed microstructural transport model is tested against literature data to show its capability to predict transport of other composite systems. The results show that the model can easily be modified and extended to other systems and research questions. Using the resistor network model provides experimentalists a new tool to fast find the range of optimized solid-state battery compositions – without the need for much computational resources.

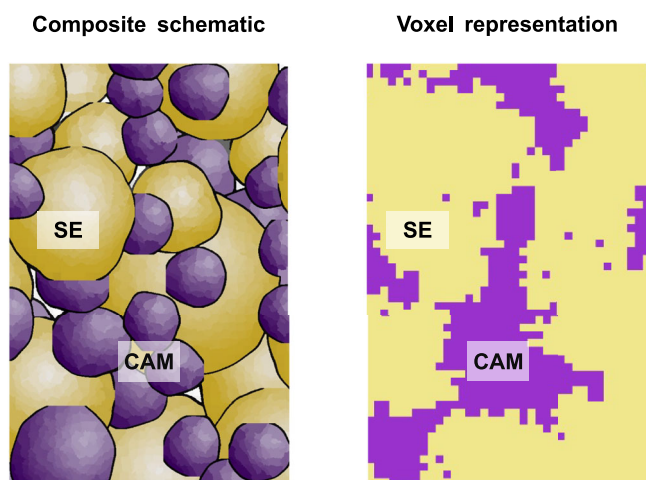


Fig. 1 | Schematic and voxel representation of a composite electrode. Comparison between a schematic composite electrode and a top view on a voxel representation of a composite consisting of cathode active material (CAM) and solid electrolyte (SE).

Results

Resistor network modeling of solid-state battery composites

When a material is subjected to a temperature gradient (∇T), heat flow occurs. According to Fourier's law (Eq. 1) the heat flux density (q) is linked to the temperature gradient by the thermal conductivity (κ) of the material³⁷:

$$q = -\kappa \nabla T \quad (1)$$

An equivalent relation for the movement of charge carriers (ions and electrons) as response to an electric field is given by Ohm's law (Eq. 2), following³⁸:

$$J = -\sigma \nabla \phi \quad (2)$$

where J , σ and $\nabla \phi$ are the electrical flux density, the electrical conductivity and the potential gradient, respectively. In the resistor network model proposed in this work we make use of these fundamental equations by applying a virtual gradient to the voxel representations of

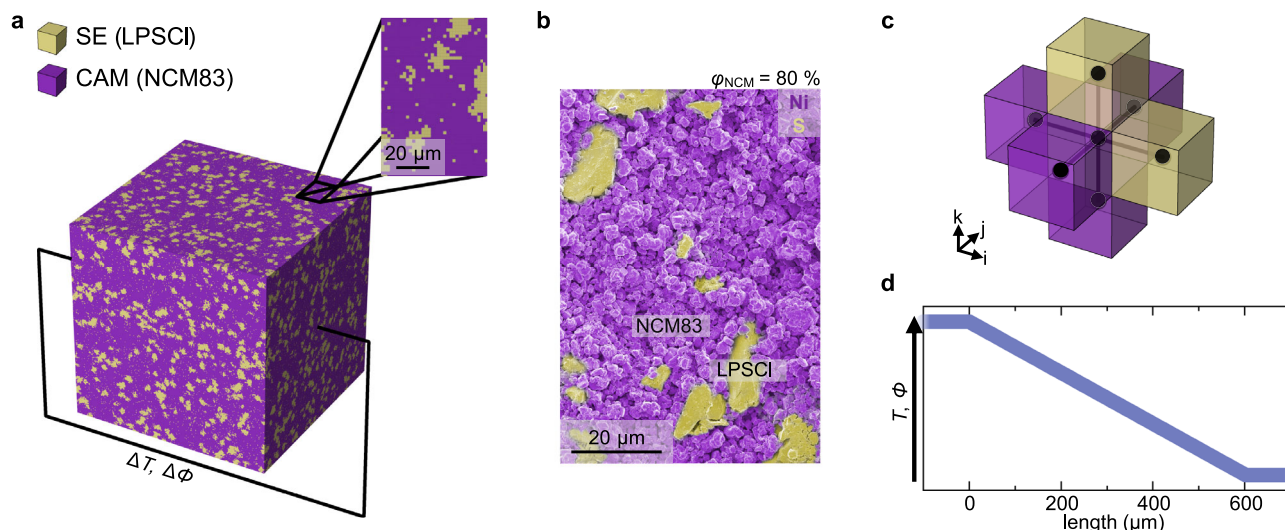


Fig. 2 | Principle of the resistor network modelling approach. **a** Voxel representation of a composite with a NCM83 volume fraction of $\phi_{\text{NCM83}} = 80\%$ and a LPSCI volume fraction of $\phi_{\text{LPSCI}} = 20\%$ generated with $300 \times 300 \times 300$ voxels. **b** Representative false-colored SEM micrograph of a composite with $\phi_{\text{NCM83}} = 80\%$ and $\phi_{\text{LPSCI}} = 20\%$. Voxels and areas colored yellow correspond to LPSCI, whereas

purple areas correspond to NCM83. **c** A representative voxel with its adjacent voxels, representing the resistor network structure and its nodes. **d** Schematic of the resulting average temperature and potential distribution along the direction of heat- and current flow in the steady state.

our composite electrodes, compute the steady states and derive effective transport properties^{39–42}.

The workflow can be described as follows (detailed description in Section S1 of the Supplementary Information): First, a microstructure consisting of $300 \times 300 \times 300$ cubic voxels is constructed. Each voxel represents a $2 \mu\text{m} \times 2 \mu\text{m} \times 2 \mu\text{m}$ domain and is assigned to either LPSCI or NCM83, leading to a total microstructure edge length of $600 \mu\text{m}$ (Fig. 2a). The number of voxels assigned to each phase is determined by the volume ratio that is investigated. A representative false-colored scanning electron microscopy micrograph of a composite is shown in Fig. 2b. In this composition, LPSCI domains ($d \approx 20 \mu\text{m}$) are embedded in a matrix of smaller NCM83 particles ($d \approx 2 \mu\text{m}$). To account for the larger solid electrolyte particles in the microstructure assembly, clustering is applied for voxels representing LPSCI (Figure S1).

Next, a resistor network is generated based on the voxel structure (Fig. 2c) considering that each voxel has either the transport properties of the SE or the CAM. With that, the conductivities of the pure phases are input parameters in the model. Each voxel center corresponds to a node in the resistor network with temperature $T_{i,j,k}$ or potential $\phi_{i,j,k}$, respectively, whereas the indices i, j and k describe the node positions in the three-dimensional structure. Each node (e.g., at position i, j and k) is linked to adjacent nodes (e.g., $i+1, j$ and k) by resistors, and the conductivity between the nodes is determined by the properties of the connected voxels. Subsequently, a virtual constant temperature or potential gradient is applied to two opposing surfaces, while zero-flux boundaries are employed at the other surfaces of the resistor network (Figure S2a) and the node temperatures or potentials are iteratively adjusted until the steady state condition is sufficiently met. From the steady state temperature or potential distribution (Fig. 2d), the effective conductivities are computed by calculating the average flux density going through the resistor network and by solving Eq. 1 or Eq. 2 for the respective conductivity in one dimension.

Exploring the electrical transport properties of solid-state battery composites

The effective ionic and electronic conductivities were measured as a function of the volume fractions of NCM83 (ϕ_{NCM83}) and LPSCI (ϕ_{LPSCI}) using electrochemical impedance spectroscopy (EIS) and direct current (DC) polarization (details in Section S4 of the Supplementary

Information). Ion-blocking contacts are employed to analyze electronic conductivities, while electron-blocking conditions are chosen to assess the ionic conductivities (Fig. 3a). A transmission line model (TLM), previously established¹² for the related NCM622-LPSCI composite system is employed to analyze the impedance results (Fig. 3a). The TLM serves as an equivalent circuit describing the electrical transport of composite cathodes by interconnected ion- and electron-conducting paths. Although not providing a complete and accurate description of the complex underlying charge transport in this composite class, it well reflects many aspects of the contemporary understanding about charge transport in electrode composites and, more importantly, can be used to correctly determine the total effective conductivities from the impedance spectra¹². Exemplary experimental results and TLM fits of a NCM83-LPSCI composite cathode with $\phi_{\text{NCM83}} = 40\%$ are shown in Fig. 3b, respectively. To further verify the ability of the TLM to determine the desired transport properties, in section S4.2 an alternative equivalent circuit often used for mixed ionic-electronic conductors⁴³ is used to evaluate the impedance data of the composite with $\phi_{\text{NCM83}} = 40\%$.

To complement the impedance results, DC polarization experiments were conducted in which the current response to different applied voltages is evaluated. Depending on whether ion- or electron-blocking contacts are employed, the resulting current can be assigned exclusively to the transport of electrons or ions, respectively. As current and the applied potential difference are linked via Ohm's law (Eq. 2), the effective electronic or ionic conductivity can be determined accordingly. An exemplary dataset for $\phi_{\text{NCM83}} = 40\%$ is shown in Fig. 3c.

After the typical experimental characterization, the effective ionic and electronic conductivities are separately calculated using the resistor network model. In the model, the experimentally assessed values for $\sigma_{\text{ion, LPSCI}}$ and $\sigma_{\text{e, NCM83}}$ were taken as input to describe the transport of voxels representing LPSCI and NCM83. Additionally, LPSCI and NCM83 were considered exclusively ion- and electron-conducting, respectively, thereby assuming $\sigma_{\text{e, LPSCI}} = \sigma_{\text{ion, NCM83}} \approx 0 \text{ mS cm}^{-1}$. This simplification does not significantly influence the obtained effective conductivities given that $\sigma_{\text{ion, NCM83}}$ ⁴⁴ and $\sigma_{\text{e, LPSCI}}$ ⁴⁵ are orders of magnitude below $\sigma_{\text{ion, LPSCI}}$ and $\sigma_{\text{e, NCM83}}$ measured in this work.

The measured and simulated effective electronic and ionic conductivities are in good agreement as shown in Fig. 3d. In line with

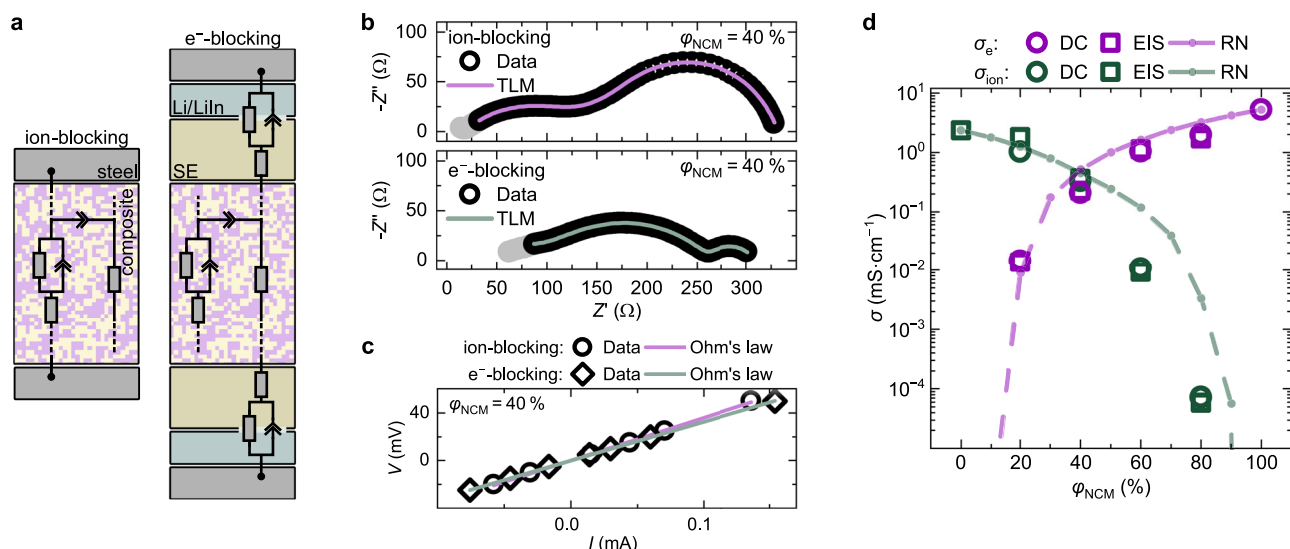


Fig. 3 | Electrical transport in composite electrodes. **a** Schematic setups used to ensure ion-blocking and electron-blocking measurement conditions respectively together with transmission line models (TLM) used to evaluate impedance data.

b Electrochemical impedance spectroscopy data (circles) measured under ion- and electron-blocking conditions are exemplary shown for a NCM83-LPSCI composite with a NCM volume fraction of 40 %. Data colored in grey are not considered during the fit (line). **c** Direct current (DC) polarization data measured under ion-blocking (circles) and electron-blocking (diamonds) conditions respectively, as well as the

corresponding fits (line) are exemplary shown for a NCM83-LPSCI composite with a NCM volume fraction of 40 %. **d** Resulting effective ionic- and electronic conductivities as a function of NCM volume fraction. Effective electronic conductivities measured via DC polarization (circles) and EIS (squares) are shown in purple, whereas effective ionic conductivities are depicted in green. Each data point corresponds to a single measurement. Effective conductivities from simulations with the resistor network model are shown as dots connected with straight dashed lines as guide to the eye.

previous results¹², the effective electronic and ionic conductivities change over orders of magnitude when the volume ratio of NCM83 to LPSCI in the composites is varied. While the effective electronic conductivities are in the range of 10^1 mS cm^{-1} to $10^{-2} \text{ mS cm}^{-1}$, the effective ionic conductivities are in the range of 10^1 mS cm^{-1} to $10^{-5} \text{ mS cm}^{-1}$ for the investigated materials. The effective ionic and electronic conductivity are closest to each other for a composition of $\phi_{\text{NCM}} = 40\%$ and a dramatic drop in the effective ionic and electronic conductivity is observed when approaching low volume fractions of LPSCI and NCM83, respectively. This behavior is also reflected by the resistor networks and is expected given the loss of percolation pathways of the respective conducting phases. Since the percolation threshold strongly depends on the microstructure, larger deviations between measured and simulated conductivities can be expected close to the threshold as only simplified, virtual microstructures are assumed in the resistor network simulations^{42,46}. Differences in the measured and simulated effective ionic conductivities for compositions with $\phi_{\text{NCM}} > 40\%$ may be attributed to this effect.

Additionally, the influence of VGCF additives on effective electronic and ionic conductivity is investigated for a composite with $\phi_{\text{NCM}} = 40\%$ and discussed in Section S2 of the Supplementary Information. While the electronic conductivity increases over two orders of magnitude upon introduction of $<2 \text{ wt.}\%$ VGCF, only minor influences on the ionic conductivity are observed.

Exploring the thermal transport properties of solid-state battery composites

Besides the electronic and ionic transport, the heat transport of composites will be decisive for the safety of a solid-state battery, and the proposed resistor network model needs to account for heat transport, too. To investigate and compare the thermal properties of NCM83, LPSCI and their composites, thermal diffusivities (D) were determined experimentally. The thermal diffusivity is a measure of how quickly temperature spreads through a material. Exceptionally low thermal diffusivities ranging from $0.18 \text{ mm}^2 \text{ s}^{-1}$ to $0.43 \text{ mm}^2 \text{ s}^{-1}$ were measured for all compositions (Figure S15).

In this work, isobaric heat capacities (C_p) are approximated by calculated isochoric heat capacities (details in the Supplementary Information Section S6). Within the investigated temperature range, all heat capacities show a steady increase with temperature (Fig. 4a) following the excitation of more vibrational modes with increasing temperatures. While LPSCI shows heat capacities ranging from $0.72 \text{ J g}^{-1} \text{ K}^{-1}$ to $1.10 \text{ J g}^{-1} \text{ K}^{-1}$, NCM83 shows lower heat capacities from $0.39 \text{ J g}^{-1} \text{ K}^{-1}$ to $0.85 \text{ J g}^{-1} \text{ K}^{-1}$. By considering the measured thermal diffusivities, calculated heat capacities and geometrical densities (Figure S18), thermal conductivities (κ) are calculated via $\kappa = \rho \cdot D \cdot C_p$. The resulting average thermal conductivities of triplicate measurements are shown in the Fig. 4b, whereby the uncertainties represent the standard deviations. The thermal conductivities are remarkably low and remain approximately constant over the measured temperature range. The room-temperature thermal conductivities are shown as a function of ϕ_{NCM} in Fig. 4c. LPSCI shows the lowest thermal conductivity in the series with $0.32 \pm 0.02 \text{ W m}^{-1} \text{ K}^{-1}$. This thermal conductivity lies within the typical range for sulfidic solid-state electrolytes^{21,30}. With a value of $0.71 \pm 0.04 \text{ W m}^{-1} \text{ K}^{-1}$, NCM83 shows the highest thermal conductivity of the investigated series in agreement with the thermal conductivities of calendared NCM electrodes reported by Gandert et al.⁴⁷ An increase in effective thermal conductivity with increasing NCM83 volume fraction is observed.

To corroborate these experimental findings, the resistor network model is utilized to simulate the thermal conductivities of the composites based on the conductivities of LPSCI and NCM83. The simulated thermal conductivities overestimate the experimental data and going forward, interfacial thermal resistances are evaluated as potential origin for the mismatch.

At perfect interfaces between different materials, interfacial thermal resistances in the range of $10^{-9} \text{ m}^2 \text{ K W}^{-1}$ to $10^{-7} \text{ m}^2 \text{ K W}^{-1}$ are caused by a mismatch in phonon structure. For imperfect interfaces at a macroscopic scale, additional effects such as porosity and surface roughness further enhance this resistance, whereas typical values lie between $10^{-6} \text{ m}^2 \text{ K W}^{-1}$ to $10^{-3} \text{ m}^2 \text{ K W}^{-1}$. Using this range of interfacial resistances as guidance, it is found empirically that better agreement

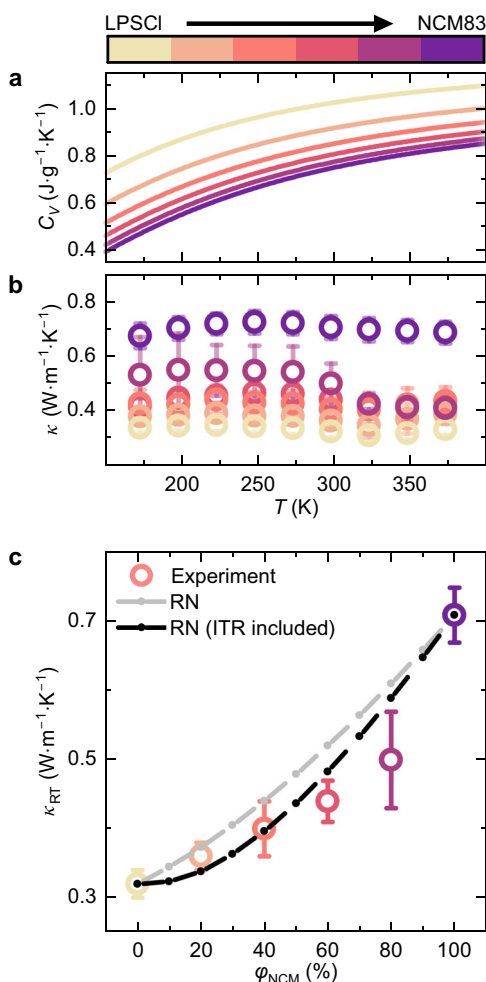


Fig. 4 | Thermal transport in composite electrodes. Data for LPSCI, NCM83 and NCM83-LPSCI composites are shown color-coded from yellow to purple with $\Delta\phi_{\text{NCM}} = 20\%$. **a** Specific isochoric heat capacities in the temperature range from 173.15 K to 373.15 K. **b** Thermal conductivities in the temperature range of 173.15 K to 373.15 K. The data (circles) shown correspond to the mean of triplicate measurements with the error bars representing their standard deviations. **c** Experimentally assessed room temperature (25 °C) thermal conductivities (color-coded circles) as a function of NCM volume fraction in comparison to simulated thermal conductivities (dots connected with dashed lines as guide to the eye) with (black) and without (grey) considering interfacial thermal resistances (ITR). The measurement data correspond to the mean of triplicate measurements with the error bars representing their standard deviations.

between simulation and experiment can be achieved considering an interfacial thermal resistance of $2 \cdot 10^{-6} \text{ m}^2 \text{ K W}^{-1}$ between the LPSCI and NCM83 domains in the resistor network model (Fig. 4c). This indicates the presence of interfacial thermal resistances between LPSCI and NCM83 providing a physically reasonable explanation for the slower increase of effective thermal conductivity with ϕ_{NCM} .

Additionally, the influence of VGCF additives on effective thermal transport is investigated for a composite with $\phi_{\text{NCM}} = 40\%$ and discussed in Section S2 of the Supplementary Information. Despite the intrinsically high thermal conductivity of carbon fibers⁴⁹, only minor influences on the effective thermal conductivity on the composites are observed in this work.

With that, this work shows that the heat transfer in the NCM83-LPSCI composite system is slow with thermal conductivities below $1 \text{ W m}^{-1} \text{ K}^{-1}$, independent of the volumetric ratio and VGCF introduction, and that based on our resistor network analysis, interfacial

thermal resistances might further lower the thermal conductivity of the composites.

Applying the resistor network model to other solid-state battery research questions

Resistor network models are widely used in various fields such as statistical physics⁵⁰, thermal barrier coatings³⁹ or in fuel cells⁵¹, to name just a few examples. To highlight the application space and predictive power of the proposed resistor network model in the case of solid-state battery composites, three literature cases are examined. An additional case study, as well as Table S3, listing the input parameters used to run the simulations are shown in section S9 of the Supplementary Information. In a study by Hendriks et al.¹³, the effective ionic and electronic conductivities of $\text{LiMn}_2\text{O}_4\text{-Li}_3\text{InCl}_6$ cathode composites were investigated (Fig. 5a). As in the NCM83-LPSCI system discussed above, significant changes in terms of charge carrier transport are observed upon varying the volumetric ratio.

Analogous to the investigated system in this work, i.e., NCM83-LPSCI composites, the CAM (LiMn_2O_4) was assumed to be exclusively electron-conducting and the SE (Li_3InCl_6) exclusively ion-conducting. The effective σ_e , LiMn_2O_4 and σ_{ion} , Li_3InCl_6 reported by Hendriks et al.¹³ were used as experimental inputs. The simulated effective conductivities are in good agreement with the experimental literature data (Fig. 5a), showing that the model is capable to describe the transport through composites of various chemistries.

Experimental results by Böger et al.³⁰ are investigated as a second case study that discuss the influence of macroscopic density (porosity) on the thermal conductivities of LPSCI (Fig. 5b). Hereby, the porous LPSCI can be considered as a two-phase system consisting of argon filled pores and solid electrolyte. Assuming $\kappa_{\text{LPSCI}} = 0.66 \text{ W m}^{-1} \text{ K}^{-1}$ for the electrolyte³⁰ and $0.017 \text{ W m}^{-1} \text{ K}^{-1}$ as thermal conductivity of argon filled pores⁵² as inputs for the resistor network model, effective thermal conductivities of porous LPSCI were simulated and are shown in Fig. 5b. Although slightly overestimating the reported effective thermal conductivities, the simulated data are generally in good agreement with the experimental results.

As a third study, the experimental results by Froboese et al.¹⁵ are evaluated, who investigated the influence of differently sized ion-blocking inclusions on the effective ionic conductivities of a PEO:LiTFSI:SiO_2 – solid electrolyte matrix (Fig. 5c)¹⁵. It was shown that for the same volume fraction of inclusions, smaller inclusion particles lead to a more pronounced decrease in the effective ionic conductivity. This effect shows more drastically for higher volume fractions of the inclusions¹⁵. To analyze this behavior using the resistor network model, the reported ionic conductivity of the PEO:LiTFSI:SiO_2 – solid electrolyte matrix was taken as a starting parameter. Ion-blocking clusters of different sizes (Fig. 5d) were constructed and used to describe the influence on the effective ionic conductivity. The simulated effective conductivities are in good agreement with the results by Froboese et al.¹⁵. In agreement with the literature results, the amplified influence of size effects with increasing volume fraction and the introduction of smaller ion-blocking clusters is captured by the resistor network model. While the general trend is reflected well, a weaker decrease in conductivity beyond inclusion fractions of approximately 30 vol.% is predicted by the resistor network model. This deviation is likely related to the simplifications of the model and the differences between the actual microstructure and the constructed voxel structure (particle shape).

These case studies highlight that the resistor network model can guide the understanding of transport and the effect of particle size in various composites of different active materials and different inorganic and polymeric solid electrolytes. Thereby, the model offers a tool to accelerate the optimization of composites, either when new chemistries are investigated, or when microstructures are designed, by providing predictive power for experimentalists. Even though the

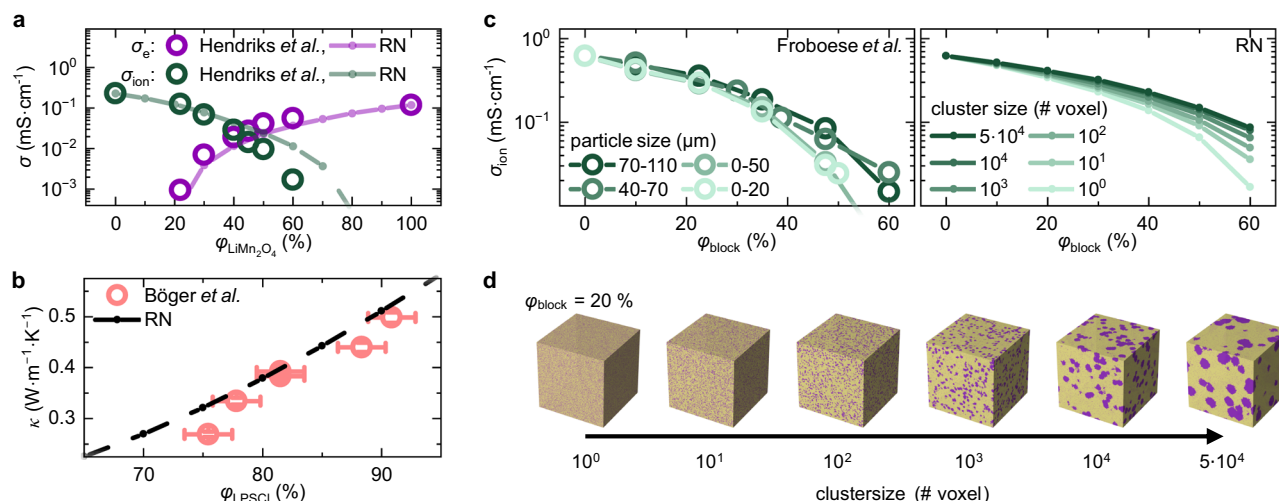


Fig. 5 | Analyzing literature case studies using resistor network models. **a** Ionic (green) and electronic (purple) conductivities reported by Hendriks et al.¹³ (circles) in comparison to simulated conductivities of the resistor network model (dots with dashed guide to the eye) as a function of LiMn₂O₄ volume fraction. **b** Thermal conductivities reported by Böger et al.³⁰ (orange circles) in comparison to results of the resistor network model (dots with dashed guide to the eye) as a function of

LPSCI volume fraction. **c** Influence of the particle size and volume fraction of an insulating second phase on the effective ionic conductivities as reported by Froboese et al.¹⁵ in comparison to the results of the resistor network model using various cluster sizes and volume fractions (ϕ_{block}) of insulating phase show good agreement with the experimental results. **d** Exemplary voxel structures for inclusions of different sizes at an inclusion volume fraction of $\phi_{\text{block}} = 20\%$.

large resistor networks computed in this work were calculated using high performance computing infrastructure, reproducible simulations can already be achieved with smaller networks (Figure S22), allowing experimentalists to compute a first guess regarding transport trends on a standard computer. For more advanced research questions such as composites without well-defined microstructures or additives that cannot be simply modelled by a voxel approach (Figure S21) however, the model runs into limitations. While the current model can predict macroscopic effective total transport properties based on composite microstructures, it does not yet provide detailed microscopic insights on charge transport mechanisms. With that, to capture complex electrode microstructures, occurring reaction pathways and chemo-mechanical influences in its complete detail, continuum models are still an important and highly valuable approach^{9,34,35}.

Discussion

In this work, the ionic, electronic and thermal transport of NCM83-LPSCI composite cathodes has been studied experimentally. While the electronic and ionic conductivities change over orders of magnitude upon changing the volume ratios of NCM83 and LPSCI, the thermal conductivities of the composite cathodes show only minor changes with composition and are remarkably low throughout all investigated samples.

In this work, a resistor network model is presented to predict the ionic, electronic and thermal transport of NCM83-LPSCI composite cathodes and experimentally validated. The model approach helps to provide a deeper understanding of the experimental transport data. Voxel structures representing the composite microstructure were generated and transport properties derived from steady-state calculations. Despite its simplicity, the simulated effective conductivities agree well with the measured data in this work and literature case studies, showing that influences of percolation, interfacial resistances and domain sizes are reflected over different active materials and solid electrolytes.

Knowledge about effective transport is crucial for electrode design considerations, but requires time-consuming, and labor-intensive measurements. This model offers guidance for experimentalists and can be used to make basic predictions for composition-dependent transport. As the model can easily be extended to include

additional concepts such as particle size distributions and particle shapes, it can streamline transport investigations in electrode composites. The simplicity of the approach sets it apart from many transport models. Hence the objective is also different: While many transport models aim to reflect exact representation of real composites, which is of immense value to deeply understand transport in such systems, the model presented in this work aims to guide experimentalists in finding optimized solid-state battery composites fast when changing the materials and particle morphologies in solid-state battery research.

Methods

Unless otherwise stated, all preparative work was carried out in a glovebox under argon atmosphere.

Synthesis

LPSCI was synthesized via a solid-state synthesis route. Therefore LiCl (Sigma-Aldrich, 99%), Li₂S (Thermo Scientific Chemicals, 99.9%) and P₄S₁₀ (Sigma-Aldrich, 99%) were weighed in stoichiometrically and hand ground for 15 min. The powder mixture was compacted using a hand press and placed in a carbon-coated quartz ampoule, which was then sealed under dynamic vacuum. After heating to 550 °C with a heating rate of 100 °C/h, the mixture was kept at this temperature for two weeks. After natural cooling to room temperature, the product was hand ground and used for further investigations.

Soft milling

LPSCI, NCM83 (MSE supplies, dried overnight at 250 °C under dynamic vacuum) and mixtures of both materials were soft milled prior to transport measurements. For composites, LPSCI and NCM83 were combined in the respective volume ratios whereby 1.86 g cm $^{-3}$ and 4.78 g cm $^{-3}$ were assumed as densities^{53,54}. Furthermore, composites with additional 1 wt.% to 5 wt.% of VGCF (Sigma-Aldrich, dried overnight at 250 °C under dynamic vacuum) were prepared. Together with spherical ZrO₂ milling media (3 mm diameter, 3.6 g), the combined materials (400 mg) were placed into ZrO₂ cups (15 mL) and mixed for 15 min at a frequency of 15 Hz using a Fritsch pulverisette 23 Mini Mill. The resulting composites were used for further investigations.

Laser flash analysis

For thermal transport measurements powder pellets were prepared. To this end, the materials were pre-compacted at 370 MPa for 3 min and subsequently isostatically pressed at 500 MPa for 60 min. Thermal diffusivities were measured in a temperature range from -100°C to 100°C with a step size of 25°C under a constant nitrogen flow (100 mL min^{-1}) using a NETZSCH LFA 467. To ensure good absorption and emission properties for all samples and to protect the samples from direct contact with the atmosphere during the brief sample transfer into the LFA, carbon coatings were applied in a nitrogen-filled glovebox. In each measurement, three thermal diffusivity values (five at -100°C) were recorded per temperature step using a MCT-detector and a ZnS sample chamber window. The mean of these values is taken as the true sample thermal diffusivity and the standard deviation between the values is taken as the measurement uncertainty. The detection time and flash intensity were automatically adjusted by the integrated software during the experiment. All measurement signals were fitted using an improved Cape-Lehmann model provided by the NETZSCH LFA Analysis 8.0.3 software to determine the respective diffusivities.

X-ray diffraction

Powder X-ray diffraction measurements were performed to confirm phase purities of the investigated materials and the absence of sample degradation during transfer into the LFA or the LFA experiment. All samples were measured in sealed quartz capillaries on a STOE STADI P with Dectris Mythen 2X 1 K detector and Ge(111) monochromator. A 2θ -range from 10° to 70° was scanned with a step size of 3° in a Debye-Scherrer geometry using Cu K α 1 radiation. Pawley refinements were performed using the TOPAS-Academic V6 software package. While a modified Thompson-Cox-Hastings pseudo-Voigt function is used to describe peak shapes, a Chebyshev function with nine variables is used to describe the background. Lattice parameters, zero error, background coefficients and peak shapes were refined.

Scanning electron microscopy and energy dispersive X-ray spectroscopy

EDX and SEM were measured to investigate sample morphology and homogeneity of LPSCI, NCM83 and their composites. The powder pellets were attached to sample holders using carbon patches. All samples were sputter coated with gold and measured on a Carl Zeiss AURIGA CrossBeam work station. An acceleration voltage of 3 kV and the In-lens detector were used for SEM measurements, whereby 20 kV and a X-Max 80 mm² detector were used as acceleration voltage and detector for the EDX measurements.

Cell assembly

The respective materials (100 mg) were filled in airtight cell casings⁵⁵ and densified for 3 min at 370 MPa. In the case of partial electronic conductivity measurements, the steel stamps of the cell casings served as ion-blocking contacts. For partial ionic conductivity measurements, electron-blocking LPSCI (80 mg) layers were added on each side of the sample. Subsequently In-foil (chemPUR, 99.99 %, 100 μm thickness, 9 mm diameter) and Li-foil (abcr, 99.8%, 1.5 mg) were placed on each side serving as Li-reservoirs. After cell assembly a constant pressure of 50 MPa was applied, and transport measurements were conducted.

Direct current polarization

Experiments were performed on a Metronohm Autolab PGSTAT302N in a climate chamber at a temperature of 25°C . Constant voltages in the range from -40 mV to 50 mV were applied for 3.5 h each and the current response was measured.

Potentiostatic electrochemical impedance spectroscopy

Measurements were conducted on a BioLogic VMP-300 at 25°C in a climate chamber at a temperature of 25°C . An equilibration step of 2 hours at open-circuit voltage was used before each measurement, whereas the voltage at the end of the equilibration time was used as quasi-stationary DC-voltage for the impedance measurement. In the frequency range from 7 MHz to 100 mHz, 15 data points were measured per decade of frequency with a perturbation voltage of 10 mV. Data analysis was performed using the RelaxIS3 software.

Data availability

Data supporting the plots and findings in this work can be accessed via <https://doi.org/10.17879/54928371863> and are made available by the data store of the University of Münster⁵⁶. Source data are provided with this paper.

Code availability

The code for resistor network calculations can be accessed via <https://doi.org/10.17879/16948580876>. It is published under a MIT license and made available through the data store of the University of Münster⁵⁷.

References

1. Janek, J. & Zeier, W. G. A solid future for battery development. *Nat. Energy* **1**, <https://doi.org/10.1038/nenergy.2016.141> (2016).
2. Janek, J. & Zeier, W. G. Challenges in speeding up solid-state battery development. *Nat. Energy* **8**, 230–240 (2023).
3. Lee, Y.-G. et al. High-energy long-cycling all-solid-state lithium metal batteries enabled by silver-carbon composite anodes. *Nat. Energy* **5**, 299–308 (2020).
4. Randau, S. et al. Benchmarking the performance of all-solid-state lithium batteries. *Nat. Energy* **5**, 259–270 (2020).
5. Yu, X., Chen, R., Gan, L., Li, H. & Chen, L. Battery Safety: From Lithium-Ion to Solid-State Batteries. *Engineering* **21**, 9–14 (2023).
6. Bradbury, R. et al. Visualizing Reaction Fronts and Transport Limitations in Solid-State Li-S Batteries via Operando Neutron Imaging. *Adv. Energy Mater.* **13**, <https://doi.org/10.1002/aenm.202203426> (2023).
7. Kimura, Y. et al. Influence of Active Material Loading on Electrochemical Reactions in Composite Solid-State Battery Electrodes Revealed by Operando 3D CT-XANES Imaging. *ACS Appl. Energy Mater.* **3**, 7782–7793 (2020).
8. Bielefeld, A., Weber, D. A. & Janek, J. Microstructural Modeling of Composite Cathodes for All-Solid-State Batteries. *J. Phys. Chem. C* **123**, 1626–1634 (2019).
9. Bielefeld, A., Weber, D. A. & Janek, J. Modeling Effective Ionic Conductivity and Binder Influence in Composite Cathodes for All-Solid-State Batteries. *ACS Appl. Mater. Interfaces* **12**, 12821–12833 (2020).
10. Kaiser, N. et al. Ion transport limitations in all-solid-state lithium battery electrodes containing a sulfide-based electrolyte. *J. Power Sources* **396**, 175–181 (2018).
11. Rudel, Y. et al. Investigating the Influence of the Effective Ionic Transport on the Electrochemical Performance of Si/C-Argyrodite Solid-State Composites. *Batteries Supercaps* **6**, <https://doi.org/10.1002/batt.202300211> (2023).
12. Minnmann, P., Quillman, L., Burkhardt, S., Richter, F. H. & Janek, J. Editors' Choice—Quantifying the Impact of Charge Transport Bottlenecks in Composite Cathodes of All-Solid-State Batteries. *J. Electrochem. Soc.* **168**, 40537 (2021).
13. Hendriks, T. A., Lange, M. A., Kiens, E. M., Baeumer, C., & Zeier, W. G. Balancing Partial Ionic and Electronic Transport for Optimized Cathode Utilization of High-Voltage LiMn₂O₄/Li₃InCl₆ Solid-State Batteries. *Batteries Supercaps* **6**, <https://doi.org/10.1002/batt.202200544> (2023).

14. Dewald, G. F., Ohno, S., Hering, J. G. C., Janek, J. & Zeier, W. G. Analysis of Charge Carrier Transport Toward Optimized Cathode Composites for All-Solid-State Li-S Batteries. *Batteries Supercaps* **4**, 183–194 (2021).
15. Froboese, L., van der Sichel, J. F., Loellhoeffel, T., Helmers, L. & Kwade, A. Effect of Microstructure on the Ionic Conductivity of an All Solid-State Battery Electrode. *J. Electrochem. Soc.* **166**, A318–A328 (2019).
16. Strauss, F. et al. Impact of Cathode Material Particle Size on the Capacity of Bulk-Type All-Solid-State Batteries. *ACS Energy Lett.* **3**, 992–996 (2018).
17. Rana, M. et al. Toward Achieving High Areal Capacity in Silicon-Based Solid-State Battery Anodes: What Influences the Rate-Performance? *ACS Energy Lett.* **8**, 3196–3203 (2023).
18. Schlautmann, E. et al. Impact of the Solid Electrolyte Particle Size Distribution in Sulfide-Based Solid-State Battery Composites. *Adv. Energy Mater.* **13**, <https://doi.org/10.1002/aenm.202302309> (2023).
19. Agne, M. T., Böger, T., Bernges, T. & Zeier, W. G. Importance of Thermal Transport for the Design of Solid-State Battery Materials. *PRX Energy* **1**, <https://doi.org/10.1103/prxenergy.1.031002> (2022).
20. Chen, R. et al. Enhancing the Thermal Stability of NASICON Solid Electrolyte Pellets against Metallic Lithium by Defect Modification. *ACS Appl. Mater. Interfaces* **13**, 18743–18749 (2021).
21. Cheng, Z. et al. Good Solid-State Electrolytes Have Low, Glass-Like Thermal Conductivity. *Small (Weinh. der Bergstr., Ger.)* **17**, e2101693 (2021).
22. Tomaszewska, A. et al. Lithium-ion battery fast charging: A review. *eTransportation* **1**, <https://doi.org/10.1016/j.etrans.2019.100011> (2019).
23. Kunz, A., Berg, C., Friedrich, F., Gasteiger, H. A. & Jossen, A. Time-Resolved Electrochemical Heat Flow Calorimetry for the Analysis of Highly Dynamic Processes in Lithium-Ion Batteries. *J. Electrochem. Soc.* **169**, 80513 (2022).
24. Morino, Y. Degradation rate at the Solid–Solid interface of sulfide-based solid Electrolyte–Cathode active material. *J. Power Sources* **541**, 231672 (2022).
25. Kim, T. et al. Critical Factors Contributing to the Thermal Runaway of Thiophosphate Solid Electrolytes for All-Solid-State Batteries. *Adv. Funct. Mater.* <https://doi.org/10.1002/adfm.202404806> (2024).
26. Lyu, P. et al. Recent advances of thermal safety of lithium ion battery for energy storage. *Energy Storage Mater.* **31**, 195–220 (2020).
27. Bates, A. M. et al. Are solid-state batteries safer than lithium-ion batteries? *Joule* **6**, 742–755 (2022).
28. Kim, T. et al. Thermal Runaway Behavior of Li₆PS₅Cl Solid Electrolytes for LiNi_{0.8}Co_{0.1}Mn_{0.1}O₂ and LiFePO₄ in All-Solid-State Batteries. *Chem. Mater.* **34**, 9159–9171 (2022).
29. Johnson, N. B. et al. Assessing the Thermal Safety of a Li Metal Solid-State Battery Material Set Using Differential Scanning Calorimetry. *ACS Appl. Mater. Interfaces*. <https://doi.org/10.1021/acsami.3c13344> (2023).
30. Böger, T., Bernges, T., Li, Y., Canepa, P. & Zeier, W. G. Thermal Conductivities of Lithium-Ion-Conducting Solid Electrolytes. *ACS Appl. Energy Mater.* **6**, 10704–10712 (2023).
31. Bernges, T. et al. Scaling Relations for Ionic and Thermal Transport in the Na + Ionic Conductor Na₃PS₄. *ACS Mater. Lett.* **4**, 2491–2498 (2022).
32. Heo, T. W. et al. Microstructural impacts on ionic conductivity of oxide solid electrolytes from a combined atomistic-mesoscale approach. *npj Comput. Mater.* **7** <https://doi.org/10.1038/s41524-021-00681-8> (2021).
33. Haruyama, J., Sodeyama, K., Han, L., Takada, K. & Tateyama, Y. Space-Charge Layer Effect at Interface between Oxide Cathode and Sulfide Electrolyte in All-Solid-State Lithium-Ion Battery. *Chem. Mater.* **26**, 4248–4255 (2014).
34. Clausnitzer, M. et al. Optimizing the Composite Cathode Microstructure in All-Solid-State Batteries by Structure-Resolved Simulations. *Batteries Supercaps* **6**, <https://doi.org/10.1002/batt.202300167> (2023).
35. Finsterbusch, M. et al. High Capacity Garnet-Based All-Solid-State Lithium Batteries: Fabrication and 3D-Microstructure Resolved Modeling. *ACS Appl. Mater. Interfaces* **10**, 22329–22339 (2018).
36. Chen, C.-F., Verma, A. & Mukherjee, P. P. Probing the Role of Electrode Microstructure in the Lithium-Ion Battery Thermal Behavior. *J. Electrochem. Soc.* **164**, E3146–E3158 (2017).
37. Dubi, Y. & Di Ventra, M. Fourier's law: insight from a simple derivation. *Phys. Rev. E, Stat., Nonlinear, and soft matter physics* **79**, <https://doi.org/10.1103/PhysRevE.79.042101> (2009).
38. Ferry, D. K. Ohm's law in a quantum world. *Sci. (N. Y., N. Y.)* **335**, 45–46 (2012).
39. Qiao, J. H., Bolot, R., Liao, H., Bertrand, P. & Coddet, C. A 3D finite-difference model for the effective thermal conductivity of thermal barrier coatings produced by plasma spraying. *Int. J. Therm. Sci.* **65**, 120–126 (2013).
40. Bolot, R., Antou, G., Montavon, G. & Coddet, C. A Two-Dimensional Heat Transfer Model for Thermal Barrier Coating Average Thermal Conductivity Computation. *Numer. Heat. Transf., Part A: Appl.* **47**, 875–898 (2005).
41. Siekierski, M. & Nadara, K. Modeling of conductivity in composites with random resistor networks. *Electrochim. Acta* **50**, 3796–3804 (2005).
42. Kirkpatrick, S. Percolation and Conduction. *Rev. Mod. Phys.* **45**, 574–588 (1973).
43. Zahnow, J. et al. Impedance Analysis of NCM Cathode Materials: Electronic and Ionic Partial Conductivities and the Influence of Microstructure. *ACS Appl. Energy Mater.* **4**, 1335–1345 (2021).
44. Amin, R. & Chiang, Y.-M. Characterization of Electronic and Ionic Transport in Li_{1-x}Ni_{0.33}Mn_{0.33}Co_{0.33}O₂ (NMC 333) and Li_{1-x}Ni_{0.50}Mn_{0.20}Co_{0.30}O₂ (NMC 523) as a Function of Li Content. *J. Electrochem. Soc.* **163**, A1512–A1517 (2016).
45. Gorai, P., Famprikis, T., Singh, B., Stevanović, V. & Canepa, P. Devil is in the Defects: Electronic Conductivity in Solid Electrolytes. *Chem. Mater.* **33**, 7484–7498 (2021).
46. Frary, M. E. & Schuh, C. A. Correlation-space description of the percolation transition in composite microstructures. *Phys. Rev. E, Stat., nonlinear, soft matter Phys.* **76**, 41108 (2007).
47. Gandert, J. C., Müller, M., Paarmann, S., Queisser, O. & Wetzel, T. Effective Thermal Conductivity of Lithium-Ion Battery Electrodes in Dependence on the Degree of Calendering. *Energy Tech.* **11**, <https://doi.org/10.1002/ente.202300259> (2023).
48. Zheng, Q., Hao, M., Miao, R., Schaadt, J. & Dames, C. Advances in thermal conductivity for energy applications: a review. *Prog. Energy* **3**, <https://doi.org/10.1088/2516-1083/abd082> (2021).
49. Ting, J.-M. & Lake, M. L. Vapor-grown carbon-fiber reinforced carbon composites. *Carbon* **33**, 663–667 (1995).
50. Yuge, Y. Three-dimensional site percolation problem and effective-medium theory: A computer study. *J. Stat. Phys.* **16**, 339–348 (1977).
51. Rhazaoui, K., Cai, Q., Adjiman, C. S. & Brandon, N. P. Towards the 3D modeling of the effective conductivity of solid oxide fuel cell electrodes: I. Model development. *Chem. Eng. Sci.* **99**, 161–170 (2013).
52. Pátek, J. & Klomfar, J. Measurement of the thermal conductivity of argon and methane: a test of a transient hot-wire apparatus. *Fluid Phase Equilibria* **198**, 147–163 (2002).
53. Deiseroth, H.-J. et al. Li₆PS₅X: a class of crystalline Li-rich solids with an unusually high Li⁺ mobility. *Angew. Chem. (Int. ed. Engl.)* **47**, 755–758 (2008).
54. Woo, S.-W., Myung, S.-T., Bang, H., Kim, D.-W. & Sun, Y.-K. Improvement of electrochemical and thermal properties of

- Li[Ni_{0.8}Co_{0.1}Mn_{0.1}]O₂ positive electrode materials by multiple metal (Al, Mg) substitution. *Electrochim. Acta.* **54**, 3851–3856 (2009).
55. Zhang, W. et al. Interfacial Processes and Influence of Composite Cathode Microstructure Controlling the Performance of All-Solid-State Lithium Batteries. *ACS Appl. Mater. interfaces* **9**, 17835–17845 (2017).
56. Ketter, L., Greb, N., Bernges, T. & Zeier, W. G. Using resistor network models to predict the transport properties of solid-state battery composites, datastore, <https://doi.org/10.17879/54928371863> (2025).
57. Ketter, L., Greb, N., Bernges, T. & Zeier, W. G. Using resistor network models to predict the transport properties of solid-state battery composites, datastore, <https://doi.org/10.17879/16948580876> (2025).

Acknowledgements

L.K. is a member of the International Graduate School for Battery Chemistry, Characterization, Analysis, Recycling and Application (BAC-CARA), which is funded by the Ministry of Culture and Science of North Rhine-Westphalia, Germany. The authors acknowledge financial support within the cluster of competence FESTBATT funded by Bundesministerium für Bildung und Forschung (BMBF; projects O3XP0597A). Simulations were carried out on the computer cluster PALMA II at the University of Münster.

Author contributions

L.K., T.B. and W.G.Z. conceived the presented idea, L.K. carried out the experiments with contributions of N.G., L.K. analyzed the data, developed the code for the resistor network simulations and performed computations, L.K. wrote the manuscript with support from T.B. and W.G.Z. All authors discussed the results and commented on the manuscript.

Funding

Open Access funding enabled and organized by Projekt DEAL.

Competing interests

The authors declare no competing interests.

Additional information

Supplementary information The online version contains supplementary material available at <https://doi.org/10.1038/s41467-025-56514-5>.

Correspondence and requests for materials should be addressed to Wolfgang G. Zeier.

Peer review information *Nature Communications* thanks the anonymous, reviewers for their contribution to the peer review of this work. A peer review file is available.

Reprints and permissions information is available at <http://www.nature.com/reprints>

Publisher's note Springer Nature remains neutral with regard to jurisdictional claims in published maps and institutional affiliations.

Open Access This article is licensed under a Creative Commons Attribution 4.0 International License, which permits use, sharing, adaptation, distribution and reproduction in any medium or format, as long as you give appropriate credit to the original author(s) and the source, provide a link to the Creative Commons licence, and indicate if changes were made. The images or other third party material in this article are included in the article's Creative Commons licence, unless indicated otherwise in a credit line to the material. If material is not included in the article's Creative Commons licence and your intended use is not permitted by statutory regulation or exceeds the permitted use, you will need to obtain permission directly from the copyright holder. To view a copy of this licence, visit <http://creativecommons.org/licenses/by/4.0/>.

© The Author(s) 2025